Biosensors and Bioelectronics 284 (2025) 117540

Contents lists available at ScienceDirect

Biosensors and Bioelectronics

journal homepage: www.elsevier.com/locate/bios

A base-stacking-driven ratiometric electrochemical biosensor using dsDNA-mediated MB-and-cholesterol co-immobilization: A model of hydrophobic versatile platform for biosensing

Lilan Xu [a,b,c,1], Guanyu Chen [a,b,c,1], Jiayan Wu [b,c], Mingzhu Chen [a,b,c], Wenlu Wang [b,c], Zhuhua Chen [a,b,c], Lifang Lin [a,b,c], Weiming Sun [b,c], Xu Yao [b,c], Jianzhong Zhang [e,*], Jinghua Chen [a,b,c,**], Xi Zhang [b,c,d,***]

[a] *Department of Pharmaceutical Analysis, The School of Pharmacy, Fujian Medical University, Fuzhou, Fujian Province, 350122, PR China*
[b] *Fujian Key Laboratory of Drug Target Discovery and Structural and Functional Research, The School of Pharmacy, Fujian Medical University, Fuzhou, Fujian Province, 350122, PR China*
[c] *Innovative Drug Research Institute, Fujian Medical University, Fuzhou, Fujian Province, 350122, PR China*
[d] *Department of Clinical Pharmacy and Pharmacy Administration, The School of Pharmacy, Fujian Medical University, Fuzhou, Fujian Province, 350122, PR China*
[e] *Department of Gastric Surgery, Fujian Medical University Union Hospital, Fuzhou, Fujian Province, 350001, PR China*

ARTICLE INFO

Keywords:
Ratiometric electrochemical biosensor
Co-immobilization
Hexanethiol self-assembled monolayer
Base-stacking
Methylene blue
Cholesterol

ABSTRACT

It remains a huge challenge to integrate the stability, reproducibility, and sensitivity of electrochemical DNA biosensors (E-sensors) for practical applications in a simplistic yet cost-effective way. In this work, we present a versatile and inclusive hexanethiol self-assembled monolayer (HT SAM) platform that strategically recruits cholesterol and methylene blue (MB) through double-stranded DNA (dsDNA) coordination, incorporating immobilization and reference functionalities onto the HT SAM. Systematically augmented anchoring sites substantially enhanced interfacial DNA probe immobilization stability and efficiency. Additionally, co-immobilized MB functions as an intrinsic reference signal, effectively mitigating the precision limitations arising from reproducibility issues inherent in conventional E-sensors. The upright dsDNA and the coaxial base-stacking promote the target-probe interactions and improve both hybridization efficiency and rate for the interface DNA probes. The tightly packed hydrophobic HT SAM facilitates $[Fe(CN)_6]^{3-}$-mediated cascade electrocatalytic amplification, further increasing E-sensor sensitivity. As a proof-of-concept, the designed base-stacking-driven ratiometric E-sensor using dsDNA-mediated MB-and-cholesterol co-immobilization successfully detected severe acute respiratory syndrome coronavirus 2 (SARS-CoV-2) N gene-related fragments, demonstrates a wide dynamic range (10 fM to 10 nM) with a low detection limit of 1.32 fM, exhibiting excellent reproducibility and selectivity. With its high detection performance, ease of operation and low cost, this E-sensor is well-suited for point-of-care testing in large-scale disease screening. Above all, the hydrophobic HT SAM as a versatile and inclusive platform combined with the ease of modification of DNA structures to recruit functional molecules and maximize their contributions is key to synergistically enhancing the overall performance of E-sensors.

1. INTRODUCTION

Electrochemical DNA biosensors (E-sensors) have gained widespread attention for their potential value in biomedical applications, such as simplicity of operation, cost-effectiveness, and suitability for miniaturization (Brahman et al. 2012, 2013, 2016a; Huang et al., 2024b; Nazir

---

* Corresponding author.

** Corresponding author. Fujian Key Laboratory of Drug Target Discovery and Structural and Functional Research, The School of Pharmacy, Fujian Medical University, Fuzhou, Fujian Province, 350122, PR China.

*** Corresponding author. Fujian Key Laboratory of Drug Target Discovery and Structural and Functional Research, The School of Pharmacy, Fujian Medical University, Fuzhou, Fujian Province, 350122, PR China.

E-mail addresses: 13705038998@139.com (J. Zhang), cjh_huaxue@126.com (J. Chen), xz@fjmu.edu.cn (X. Zhang).

[1] These authors contributed equally.

https://doi.org/10.1016/j.bios.2025.117540
Received 16 January 2025; Received in revised form 8 April 2025; Accepted 1 May 2025

et al., 2022; Tu et al., 2023; Wang et al. 2022a, 2022b). Nevertheless, despite significant development, challenges related to stability, reproducibility, and sensitivity hinder the wider adoption of E-sensors as analytical devices in clinical settings (Li et al., 2016; Myres and Harris, 2023). To translate proof-of-principle studies into clinical sample detection, there is an urgent need to overcome these issues to meet clinical requirements.

The construction of traditional E-sensors typically involves the immobilization of thiol-functionalized DNA at the gold electrode interface, the passivation of non-DNA regions using 6-mercaptohexanol (MCH), and interactions between surface-immobilized DNA and complementary oligonucleotides, small molecules, or proteins in solution (Lao et al., 2005; Shaver and Arroyo-Currás, 2022). However, gold-thiol bonding can only immobilize thiol-functionalized molecules and has limited functionality of electrode interface. Additionally, the progressive degradation of the bioelectronic interface or the shedding of thiol-labeled DNA probes due to competition with MCH further restrict the application of MCH (Li et al., 2021; Shaver et al., 2020). Previously, to address these issues, we constructed a hexanethiol self-assembled monolayer (HT SAM), whose tightly and orderly packed hydrophobic alkyl chains resisted the progressive degradation of the monolayer, and a cholesterol-modified DNA probe was used as an example to immobilize on HT SAM by hydrophobic interaction, which effectively preventing the shedding of the DNA probe caused by the competition between thiols (Chen et al., 2022). However, relying on a single anchoring point via single-stranded DNA (ssDNA) provides insufficient structural stability for probe DNA immobilization. Additionally, cholesterol molecules are only employed for DNA immobilization, with their functional application remaining singular and underutilizing the versatility of the electrode interface.

Multiple anchoring points may offer ideas to solve the above problems (Kuralay et al., 2012; Li et al., 2002; Singhana et al., 2013; Wang et al., 2012). Fortunately, the strict complementary base pairing principle enables DNA molecules to spontaneously form highly organized, structured, functional, information-rich DNA structures, such as double-stranded DNA (dsDNA) or framework DNA (Brahman et al., 2016b; Chen et al., 2024; Huang et al., 2024a; Li et al., 2020; Lu et al., 2023; Zhang et al., 2018). The structural “tentacles” on these 2D or 3D nanostructures become accessible anchoring points for the multiple modifications of molecules, thereby enhancing the immobilization of DNA probes (Wu et al., 2023). Unlike the limitation of the gold-thiol bonding for immobilization, the hydrophobic nature of our HT SAM fittingly allows for the immobilization of any functional molecules with hydrophobicity, such as methylene blue (MB) (Romanò et al., 2024; Zeng et al., 2024), DSPE-PEG (Chang et al., 2023), anthraquinone (Li et al., 2016), pyrene (Zhang et al., 2023), acridone (Xia et al. 2019, 2021), and others (Zhao et al., 2021). These hydrophobic molecules not only can increase the probe immobilization strength but also play a role in different conventional electrochemical biosensors. For example, MB, anthraquinone, DSPE-PEG and pyrene have electrochemical activity and can be used as the internal reference in E-sensors (Chang et al., 2023; Li et al., 2016). Acridone has the features of electrochemical, two-photon fluorescence, visible-light-induced oxidase mimic, and photoelectrochemistry (PEC) activities, which can be used in the development of multi-mode detection (Xia et al., 2019). Therefore, aside from immobilization, the rational integration of those hydrophobic functional molecules can certainly improve the overall performance of E-sensors. That is, DNA work as a “mediator”, systematically recruiting various molecules and bringing the multifunctional ensemble onto the HT SAM, while the HT SAM serves as a versatile and inclusive platform, accommodating each component to maximize its contribution in the E-sensor.

Here, we use dsDNA as a straightforward example, which provides several advantages. 1) The two strands of dsDNA not only inherently provide two anchoring points to strengthen the stability of immobilization but also enable two components to function simultaneously. 2) We use cholesterol and MB as model components, where MB serves as a built-in correction analysis tool for better reproducibility and precision (Fig. S1). 3) The rigidity of dsDNA, combined with the electrostatic repulsion between DNA strands, maintains an upright DNA conformation, thereby facilitating the enhancement in target capture efficiency. 4) The viscous ends and double-helix structure of dsDNA promoted coaxial base-stacking at both ends, leading to a substantial enhancement in the target capture rate (Chen et al., 2023; Cheng et al., 2023). 5) More subtly, the tightly packed, hydrophobic HT SAM enables the $[Fe(CN)_6]^{3-}$-mediated cascade electrocatalytic amplification reaction, making it suitable for the highly sensitive detection of low-abundance targets in biological samples.

In order to validate the performance of the proposed approach in clinical practice, SARS-CoV-2 N gene-related fragments (T) was selected as the model analyte. Benefiting from the MB-and-cholesterol co-immobilization (MB-Chol co-immobilization), the dsDNA capture probe, and amplification reactions, the proposed biosensor provided outstanding amplification efficiency and sensitivity of the electrochemical assay with a detection limit down to 1.32 fM. The ratiometric E-sensor has the advantages of simple operation, low cost, rapid reaction and high amplification efficiency, and holds great potential for large-scale disease screening.

2. Experiment section

2.1. Materials

SARS-CoV-2 mainly contains S gene, E gene, M gene, N gene, replicase complex (ORF1ab), 5 untranslated regions (UTR) and multiple unrecognized non-structural open reading frames (Mohammadniaei et al., 2021). Since the nucleocapsid protein (N protein) is the most conserved and stable protein structure in SARS-CoV-2, it has the least feasibility of mutation and has good specificity. Therefore, the N gene-related fragment corresponding to the N protein was selected as the detection target. Other related DNAs were designed according to its sequence. All the oligonucleotides were purchased from Shanghai Sangon Biotech and TaKaRa Biotechnology Co., Ltd. All of them were purified by high performance liquid chromatography (HPLC). The relevant sequence information is listed in Table S1. The HT was obtained from Shanghai Macklin Biochemical Co., Ltd. Potassium ferricyanide ($K_3Fe(CN)_6$), glycerol ammonium persulfate (APS), tetramethylethylenediamine (TEMED) were purchased from Sinopharm Chemical Reagent Co., Ltd. All chemical reagents are analytically pure, and the experimental water is ultrapure water purified by the Millipore Milli-Q system (18.2 MΩ/cm).

2.2. DNA design and theoretical fitting

The theoretical structure of DNA was fitted by NUPACK software (Zadeh et al., 2011), followed by an analysis of its thermodynamic parameters and theoretical equilibrium concentration. The fitting nucleic acid type was DNA mode, the fitting temperature was room temperature (25°C), the initial concentration of each nucleic acid sequence was set to 1 μM, and the concentrations of Na^+ and Mg^{2+} were 0.0500 M and 0.0125 M, respectively.

2.3. Polyacrylamide gel electrophoresis (PAGE) characterization

Capture probe (Cp), auxiliary probe (Ap), signal probe (Sp), T and their mixed sequences were diluted with DNA fixation buffer (prepared with 10 mM Tris, 1 mM $EDTA\cdot2Na\cdot2H_2O$, 50 mM NaCl, and 1 mM $MgCl_2$, with pH adjusted to 8) to the desired concentrations, then were heated at 95°C for 5 min, cooled to room temperature and stored at 4°C. Subsequently, 10 μL of the prepared samples were combined with 2 μL of 50% glycerol, and the mixture was subjected to electrophoresis using a Hoefer SE300 miniVE vertical electrophoresis apparatus. The process utilized a 10% non-denaturing polyacrylamide gel in a 1 × TAE buffer (prepared with 10 mM Tris, 1 mM EDTA·2Na·2H_2O, 12.5 mM $(CH_3COO)_2Mg·4H_2O$), at a voltage of 120 V for 110 min. After electrophoresis, the gel was stained with 0.1% Stains-All and then imaged with a scanner.

2.4. Electrode treatment and the construction of the ratiometric E-sensor

Electrochemical measurements were performed with a CHI 660 electrochemical workstation (Shanghai Chenhua Instrument Co., Ltd.). The surface of the gold electrode (GE) was polished with 0.30 and 0.05 μm alumina and ultrasonically cleaned with deionized water and anhydrous ethanol for 1 min, respectively. After nitrogen drying, the GE was scanned by cyclic voltammetry (CV) in 0.5 M H_2SO_4 until the curves were stable. The scanning potential of CV ranged from −0.35 to +1.50 V, and the standing time, scanning rate, and sampling interval were 2 s, 0.1 V/s, and 1 mV, respectively.

The polished GE was immersed in 5 mM HT for 1 h at room temperature. Afterward, 4 μL of 0.5 μM MB-Chol co-modified Cp-Ap dsDNA was added to HT assembly electrode for 1 h at room temperature, creating the dsDNA-anchored electrode. Next, 4 μL of 2 μM Sp and T mixed solution was dropped onto the above electrode to construct the ratiometric E-sensor. After incubation for 30 min, the GE was cleaned with deionized water and dried with nitrogen. Finally, the prepared electrode was placed in 10 mM $K_3Fe(CN)_6$ solution for electrochemical detection. Square wave voltammetry (SWV) was performed for detection of the signal. The scanning potential of SWV ranged from −0.5 to 0.7 V, and the amplitude, frequency, and quiet time were 0.025 V, 50 Hz, and 2 s, respectively.

2.5. Sample recovery experiment

The Cp-Ap dsDNA modified electrode was prepared according to the above method. Next, T and Sp were dissolved in PBS-diluted saliva samples containing RNAase inhibitors and then dropped on the Cp-Ap dsDNA modified electrode. Electrochemical detection was subsequently performed in 10 mM $K_3Fe(CN)_6$ solution, and SWV signals were collected to calculate the recovery rates. Saliva samples were collected from Fujian Medical University.

3. Results and discussion

3.1. Feasibility of MB for DNA probes immobilization

MB is arguably one of the most widely used redox reporters in E-sensors. Especially, it can serve as a reference for calibrating the sensing ratio in ratiometric E-sensor (Deng et al., 2017; Wan et al., 2023; Zhang et al., 2019). Coincidentally, its hydrophobic, planar structure allows for the immobilization on HT SAM, enabling the immobilization of MB-modified DNA probes. The inclusivity and versatility of HT SAM platform make it possible to “repurpose” MB, using it both as a redox reporter and as an immobilization anchor. To assess this, we calculated the binding energy (E_{ad}) between MB and HT by density functional theory (DFT). As depicted in Fig. S2, the E_{ad} of MB-HT complex was −35.73 kcal/mol, where a negative E_{ad} value indicates a favorable

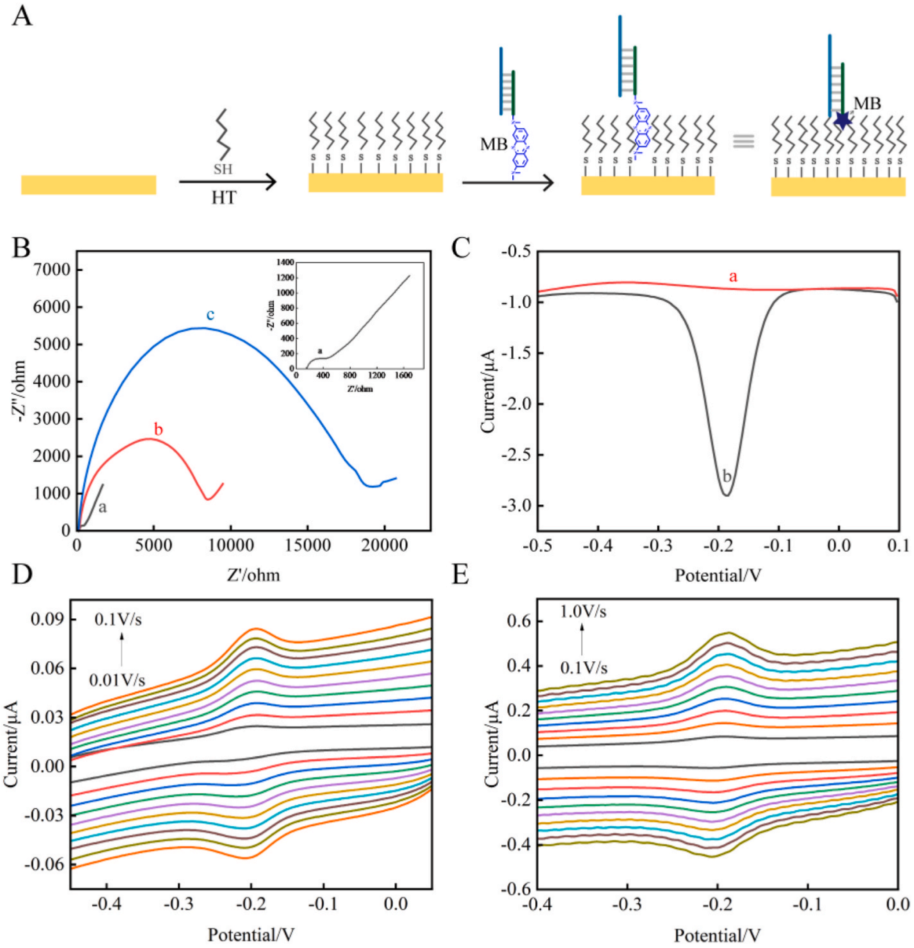

Fig. 1. (A) Immobilization process of MB-modified DNA probe. (B) EIS feasibility characterization of MB-modified DNA probe immobilization (curve a: BGE, curve b: GE/HT, curve c: GE/HT/MB-modified DNA). (C) SWV feasibility characterization of MB-modified DNA probe immobilization, curve a: GE/HT, curve b: GE/HT/MB-modified DNA. CV of GE/HT/MB-modified DNA in PBS buffer at (D) lower (0.01–0.1 V/s) and (E) higher scan rates (0.1–1.0 V/s).

binding between MB and HT.

We then validated experimentally the capacity of MB to immobilize DNA probes. The process of MB-modified DNA probe immobilization is illustrated in Fig. 1A. Electrochemical impedance spectroscopy (EIS) was used to characterize its feasibility. As shown in Fig. 1B curve a, the bare electrode (BGE) exhibited a minimal electron-transfer resistance (R_{et}), suggesting its excellent conductivity. After the assembly of HT on the electrode surface, electron transfer was hindered, leading to a substantial increase in R_{et} (curve b). This was attributed to the tight packing of HT at the electrode interface, which significantly hindered the electron transfer between $[Fe(CN)_6]^{3-/4-}$ and the electrode interface. Due to the repulsion of $[Fe(CN)_6]^{3-/4-}$ by negatively charged DNA phosphate backbone, the addition of MB-modified DNA resulted in a further increase in R_{et} (curve c), confirming the successful assembly of MB-modified DNA on the electrode surface. The results of CV were consistent with EIS (Fig. S3), both confirming the feasibility of MB-modified DNA assembly on HT SAM. In addition, we observed that the MB-modified DNA assembled electrode showed an obvious MB redox peak at about −0.2 V (Fig. 1C, curve b), while the HT-assembled electrode did not (Fig. 1C, curve a). This was attributed to the immobilization of MB-modified DNA onto the electrode interface, further confirming the feasibility of using MB for DNA probe immobilization and as an internal reference signal of the electrode.

We also studied the electrochemical behavior of MB on HT SAM to further verify the feasibility of MB for DNA probe immobilization. As shown in Fig. 1D, within the lower scan rate range (0.01–0.1 V/s), the redox peak of MB increased with the scan rate, while maintaining an excellent symmetry and no significant shift in peak potential. Additionally, the oxidation peak current of MB correlated linearly with the scan rate (Fig. S4A). These findings were consistent at higher scan rates (0.1–1.0 V/s) (Fig. 1E, Fig. S4B), suggesting that the electron transfer process is predominantly governed by adsorption rather than diffusion, highlighting the strong affinity of MB-modified DNA for HT SAM.

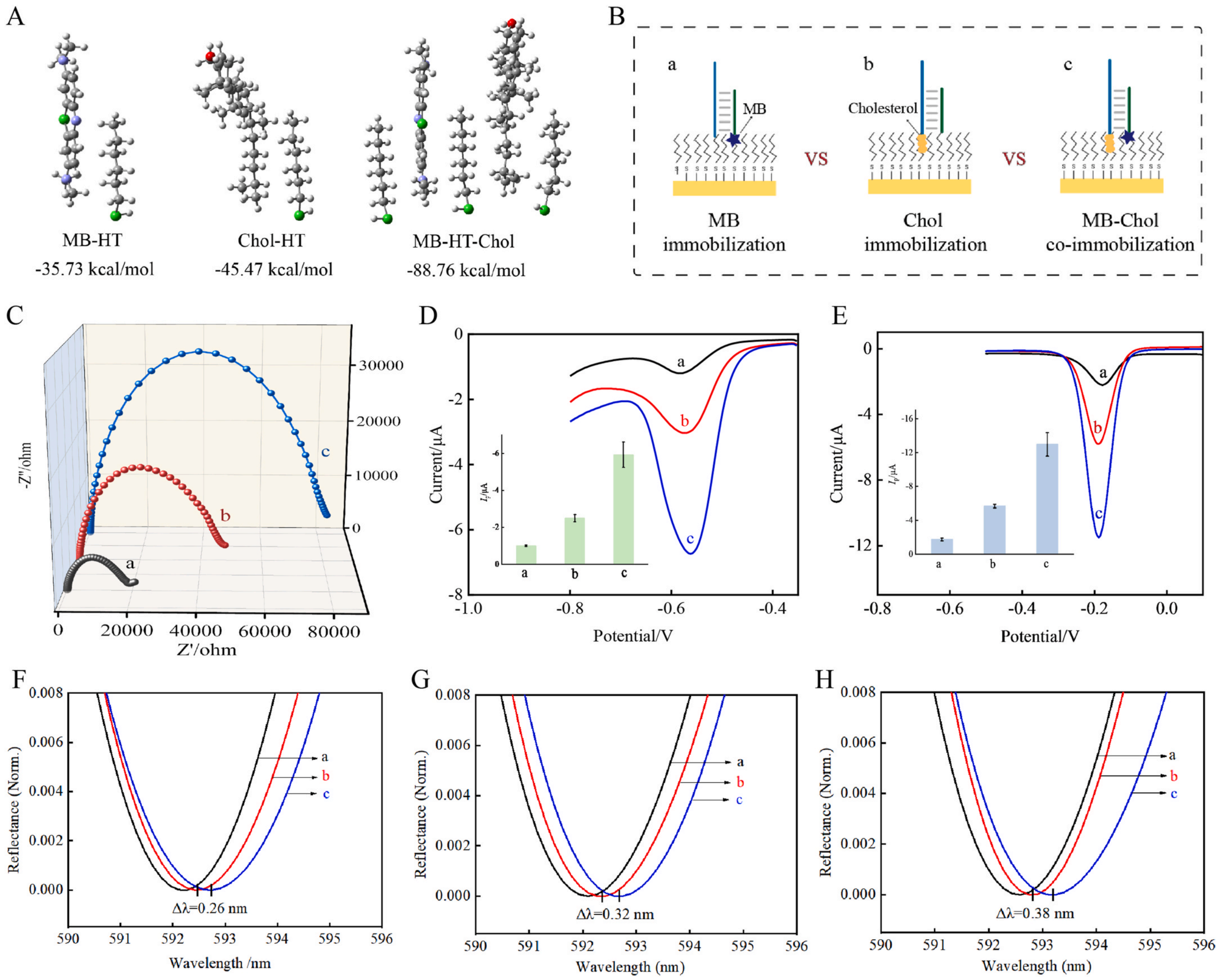

Fig. 2. (A) The geometric structure and the E_{ad} value of MB-HT, Chol-HT, MB-HT-Chol complexes (the grey, white, purple, green, and red spheres represent carbon, hydrogen, nitrogen, sulfur, and oxygen atoms, respectively). (B) The schematics of various immobilization models and their (C) EIS, (D) DOX intercalates, and (E) MB adsorption (the illustration is a histogram of the SWV peak current, $n = 3$) characterizations: (a) MB immobilization, (b) Chol immobilization, (c) MB-Chol co-immobilization. SPR spectra of (F) MB immobilization, (G) Chol immobilization, (H) MB-Chol co-immobilization: curve a: bare substrate, curve b: bare substrate/HT, curve c: bare substrate/HT/MB-modified (Chol-modified or MB-Chol co-modified) DNA. (For interpretation of the references to colour in this figure legend, the reader is referred to the Web version of this article.)

3.2. Construction of MB-Chol co-immobilization and characterization of its immobilization efficiency

MB, capable of intercalating into the well-ordered HT SAM and displaying distinct electrochemical responses, can serve as a reference for calibrating the sensing ratio in ratiometric E-sensor. Therefore, we proposed to use MB as an auxiliary molecule, cooperate with cholesterol to achieve multi-anchor immobilization of DNA on HT SAM and introduce MB reference function to improve the performance of E-sensor. To verify this, DFT theoretical calculation was used to assess the binding affinity of different molecules with HT. As depicted in Fig. 2A, the MB-HT complex had an E_{ad} of -35.73 kcal/mol, which was less negative compared to the Chol-HT complex's E_{ad} of -45.47 kcal/mol, suggesting that the binding ability of MB to HT was weaker than that of cholesterol to HT. This may be due to the presence of hydrophilic groups, such as sulfonic acid and amino groups in MB, weakens the strength of MB and HT. Furthermore, the E_{ad} of the MB-HT-Chol complex was calculated to be -88.76 kcal/mol, significantly more negative than either the MB-HT or Chol-HT complexes. This indicated that binding energy of HT with MB and cholesterol is stronger than that of HT with either MB or cholesterol alone, and that the strengths of MB and cholesterol complement each other, facilitating a the synergistic effect between the two. The interaction region indicator (IRI) was used to model the van der Waals forces between the molecules (Fig. S5). The green regions between molecules represent the presence of these forces. The van der Waals forces in the MB-HT-Chol complex were significantly higher than those in either the MB-HT or Chol-HT complexes. The results of IRI were consistent with the DFT calculations, supporting the synergistic strategy of cholesterol and MB to strengthen the immobilization.

We then constructed three immobilization models—MB immobilization, cholesterol immobilization (Chol immobilization), and MB-Chol co-immobilization (Fig. 2B)—to compare the amount of DNA probes at the electrode interface using different immobilization methods, in order to validate that the co-immobilization of MB and cholesterol can enhance the immobilization efficiency of DNA probes. EIS was first used to characterize this process. As depicted in Fig. 2C, the R_{et} for MB immobilization (curve a) was the lowest, followed by Chol immobilization (curve b), with the highest R_{et} observed for MB-Chol co-immobilization (curve c). This suggested that the MB-Chol co-immobilization resulted in a higher amount of DNA attached to the electrode interface, thereby increasing the immobilization efficiency.

Doxorubicin (DOX), which intercalates into the DNA double strand and exhibits a distinct redox peak, was used to further indicate the immobilization efficiency by comparing the peak currents generated by DOX under different immobilization methods. A larger redox peak current for DOX correlates with a greater amount of DNA attached to the electrode. As shown in Fig. 2D, the peak current of MB immobilization was the smallest (curve a), followed by Chol immobilization (curve b), with the highest peak current observed for MB-Chol co-immobilization (curve c).This indicated that the electrode interface with MB-Chol co-immobilization had the highest amount of DNA attached and thus the highest DNA probe immobilization efficiency. We also further validated the feasibility of enhancing immobilization efficiency by the peak current of MB (MB and DNA phosphate backbone electrostatic adsorption binding). The results for MB adsorption were consistent with those for DOX (Fig. 2E), further confirming that the MB-Chol co-immobilization improved DNA immobilization efficiency at the electrode interface.

Additionally, we used surface plasmon laser resonance (SPR) technology to verify the enhancement of DNA probe immobilization efficiency by the MB-Chol co-immobilization at other gold substrate interface. As depicted in Fig. 2F–H, the SPR spectra for various DNA probe immobilization methods exhibited significant red shifts, indicating successful DNA immobilization on the gold substrate. The MB-Chol co-immobilization showed the most significant red shift in the spectra, with the highest coverage rate observed (Fig. S6). This suggested that MB-Chol co-immobilization resulted in a higher amount of DNA attached to the gold substrate, consistent with the findings on the electrochemical interface, and demonstrated a certain degree of universality of this enhanced DNA probe immobilization method.

3.3. Validation of immobilization stability

To investigate whether the MB-Chol co-immobilization enhances the temporal stability of DNA probes at the electrode interface, we compared the changes of DOX peak current values (I_p) of the above three assembled electrodes with different immobilization methods before and after 2 weeks in PBS solution at 4°C, and calculated the change of I_p decay rate to reflect the shedding of DNA at the electrode interface. The results, shown in Fig. S7, revealed that the I_p for MB immobilization and Chol immobilization assembled electrode were reduced by 35.6% and 24.8% respectively, whereas the MB-Chol co-immobilization assembled electrodes only showed a 16.2% reduction. This suggested that the temporal stability of DNA probe immobilization was enhanced by MB-Chol co-immobilization.

Furthermore, since the preparation of most E-sensors involves multiple assembly steps at the electrode interface, with the requirement of deionized water rinsing after each step, continuous rinsing can lead to DNA probe shedding, compromising E-sensor performance. To confirm that the MB-Chol co-immobilization enhances the stability of DNA probes during continuous rinsing, we employed a MB labeling method to construct three immobilization models (Fig. 3A). The absolute change in current of MB reflected the shedding of DNA probes at the interface, which then reflected the stability change of DNA probes immobilization under continuous rinsing. After each 30-s rinse, SWV scans were conducted at room temperature. As depicted in Fig. 3B, after 10 rinse cycles, the I_p of MB immobilization and Chol immobilization assembled electrodes decreased by 89.1% and 77.0%, respectively. The MB-Chol co-immobilization assembled electrodes exhibited superior stability, with only a 39.1% reduction in the signal. Considering that MB can also be embedded in the HT SAM to achieve the immobilization of DNA probes, we also conducted experiments to exclude the interference of MB in the Chol immobilization model (see Fig. S8 for details). Additionally, MB-Chol co-immobilization electrodes exhibited a significantly higher number of rinsing cycles, compared to the electrodes immobilized with either MB or cholesterol alone, before the current reached 0 μA. These results indicated that MB-Chol co-immobilization enhanced the stability of the DNA probe with continuous deionized water rinsing.

The MB-Chol co-immobilization also showed significantly better stability during repeated electrochemical interrogations. As observed in Fig. 3C–E, the I_p of MB immobilization and Chol immobilization assembled electrodes decreased by 27.5% and 16.9% after 50 consecutive CV scans, respectively. In contrast, MB-Chol co-immobilization assembled electrodes exhibited a much smaller decrease of only 8.5% in the I_p, demonstrating the highest stability when subjected to continuous voltametric inquiries.

3.4. Characterization of hybridization efficiency

Coaxial base-stacking plays a significant role in the thermodynamic stability of DNA hybridization, which can influence both the efficiency and rate of hybridization (Cai et al., 2011; Chang et al., 2023; Chen et al., 2023; Hu et al., 2018). Compared to ssDNA, the double helix and sticky end structure of dsDNA make it more favorable for coaxial base-stacking. To investigate this, we constructed a model for ssDNA and dsDNA hybridization and evaluated their hybridization efficiency (Fig. S9). As shown in Fig. S10, the peak current of MB for dsDNA was higher than that for ssDNA, indicating that more MB-modified DNA (T probe) hybridized with dsDNA. Based on the number of T on the interface, we calculated their hybridization efficiency. As expected, the calculated hybridization efficiency between T and dsDNA at the interface was 53.08%, a significant improvement over the 36.32% observed with ssDNA (Fig. S11).

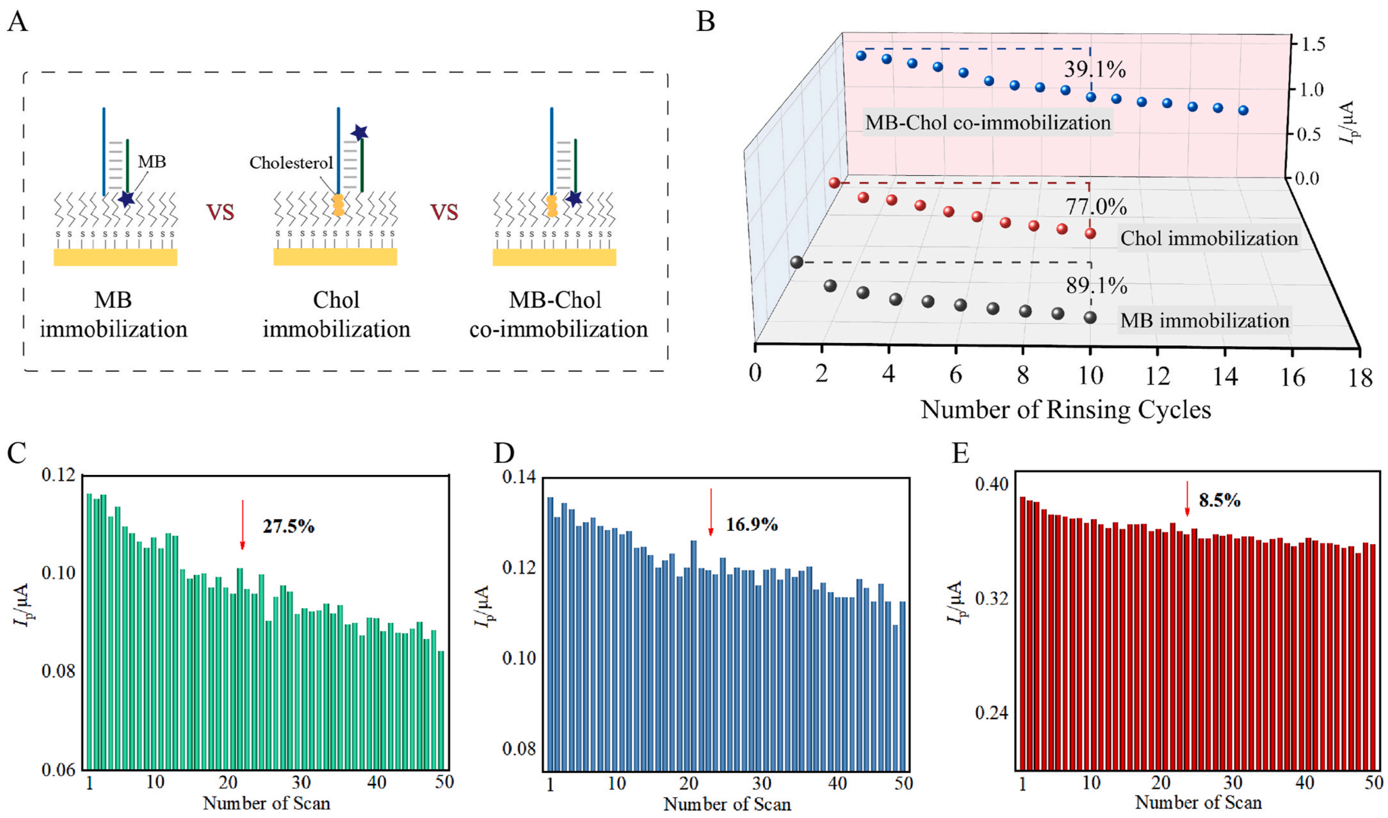

Fig. 3. (A) The schematics of various immobilization models based on MB labeling. (B) Continuous flushing stability characterization of various immobilization models. Histograms of continuous 50 CV scans with various immobilization models: (C) MB immobilization, (D) Chol immobilization, (E) MB-Chol co-immobilization.

Next, the hybridization dynamics of dsDNA and ssDNA with T were characterized. As depicted in Fig. S12 A, the peak currents of both modes increased continuously during hybridization until reaching a plateau. Notably, the dsDNA mode reached a higher plateau more rapidly than the ssDNA mode. To quantitatively assess the hybridization rate of different modes, a rate curve was plotted based on the relationship between peak current and time (Fig. S12 B). The dsDNA mode demonstrated a significantly faster rate of 6.27×10^8 molecules/(cm^2·s), compared to 1.68×10^8 molecules/(cm^2·s) for the ssDNA mode Fig. S12 B.

Additionally, both strands in dsDNA can produce coaxial base-stacking when appropriate DNA fragments are present. Thus, by leveraging base-stacking in both strands, it can effectively improve the thermodynamic stability of DNA hybridization on electrode surface. To verify this, the secondary structure free energies of different DNA structures (Fig. S13A) were calculated by NUPACK software (Zadeh et al., 2011). The DNA structure with coaxial base-stacking on both strands has a more negative energy (−64.53 kcal/mol) than the one with stacking at one end (−42.08 kcal/mol), indicating a more stable duplex structure. Experimental validation further supported this. As shown in Fig. S13B, the MB current signal of DNA structure with coaxial base-stacking on both strands was significantly higher than that with stacking at one end, indicating it was more stable. The results suggested that the upright conformation of the dsDNA, along with the coaxial base-stacking in both strands, enhanced the reaction efficiency and rate of the E-sensor.

3.5. *Feasibility characterization of ratiometric signal amplification*

Enhancing the electron transfer ability of the redox reporter can increase the sensitivity of the E-sensor. As known, the $[Fe(CN)_6]^{3-}$-mediated electrocatalytic signal amplification reaction continuously regenerates the redox labels through electron transfer, and the shielding of the electron transfer reaction between $[Fe(CN)_6]^{3-}$ and the electrode interface is a prerequisite for this amplification reaction. Notably, the hydrophobic property of the tightly packed HT SAM can effectively achieve this shielding (Fig. S14).

We then verified the feasibility of MB electrocatalytic reaction on HT SAM. The mechanism of the reaction, shown in Fig. S15A, involves electrons flowing from the electrode interface to the MB^+, generating leuco-methylene blue (LB^+), the reduced form of MB^+. LB^+ then reduces solution-borne $[Fe(CN)_6]^{3-}$, allowing more electrons to flow to MB^+, and the catalytic cycle continues. The current of MB showed a 4.8-fold increase in $[Fe(CN)_6]^{3-}$ (Fig. 4A curve a) than in the PBS buffer (Fig. 4A curve b), demonstrating the success of electrocatalytic amplification of the MB response at the HT-assembled electrode. Similarly, as shown in Fig. S15B, the catalytic mechanism of Fc is analogous to that of MB. The current of Fc in $[Fe(CN)_6]^{3-}$ (Fig. 4B curve a) was significantly larger than in the PBS buffer (Fig. 4B curve b).

It is worth to noting that both Fc and MB are often selected as signal molecules for ratiometric electrochemical sensing platforms due to their wide peak potential differences. To take advantage of the capability of electrocatalytic reaction, we further investigated the simultaneous catalytic reaction of MB and Fc at HT-assembled electrode. As shown in Fig. 4C, at about −0.2 V and 0.4 V, distinct oxidation peaks of MB and Fc were observed, respectively, and the current response of MB and Fc in $[Fe(CN)_6]^{3-}$ (curve a) was significantly higher than that in PBS buffer (curve b), showing the promise in ratiometric biosensors. Even more, we observed that the current signal generated by Fc in the simultaneous amplification of MB and Fc was higher than that in the case of sole Fc (Fig. 4D, Fig. S16). The electrocatalytic reaction mechanisms of MB, Fc and Fe^{2+}/Fe^{3+} involved in the biosensor are detailed as follows: Electrons flow from the electrode interface to MB and Fc on the DNA probe, generating LB^+ and Fc^+. LB^+ reduces $[Fe(CN)_6]^{3-}$ in the solution to form

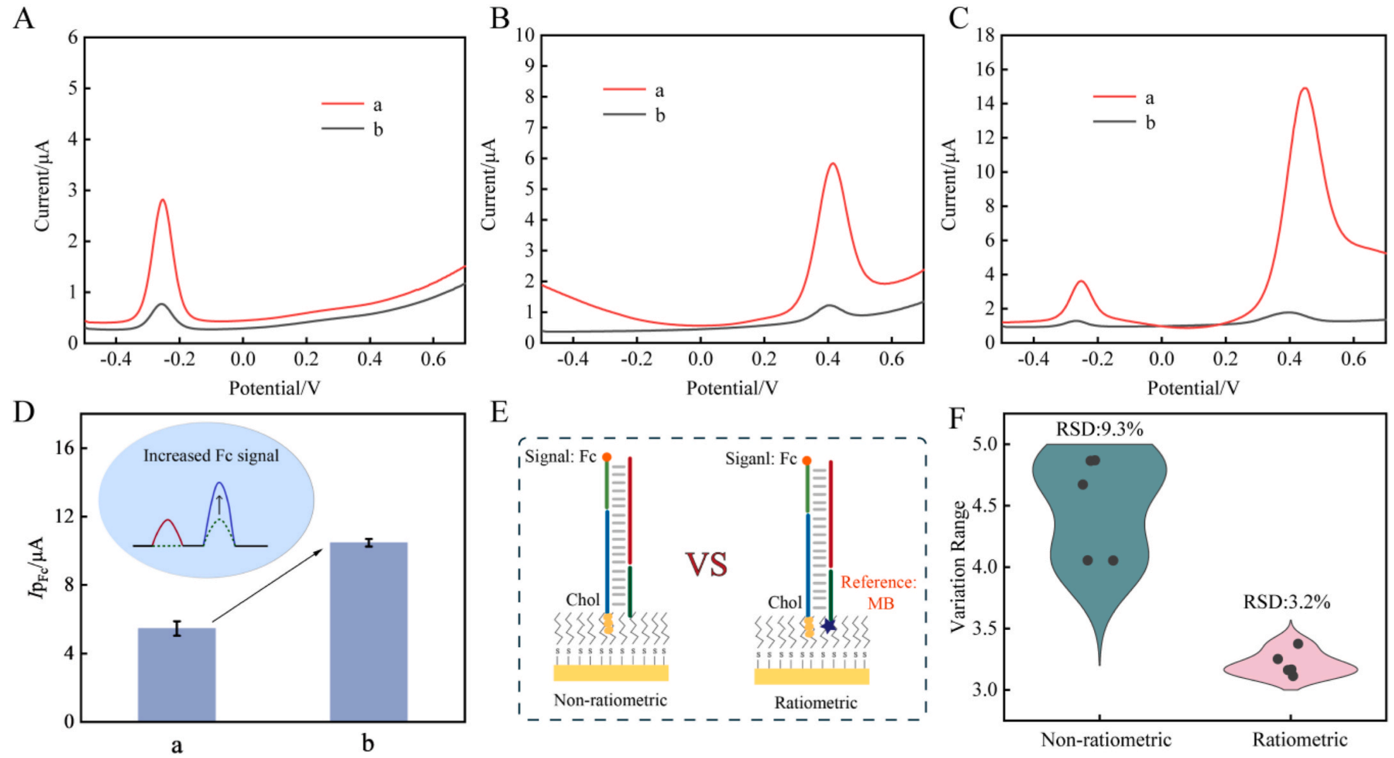

Fig. 4. SWV characterization of (A) MB signal amplification, (B) Fc signal amplification, (C) MB and Fc simultaneous signal amplification: curve a: after catalysis; curve b: before catalysis. (D) Comparison of Fc catalytic current in (a) traditional electrocatalysis and (b) cascade electrocatalysis ($n = 3$). (E) The diagrams of non-ratiometric and ratiometric E-sensors. (F) The degree of signal drift of non-ratiometric and ratiometric E-sensors ($n = 5$).

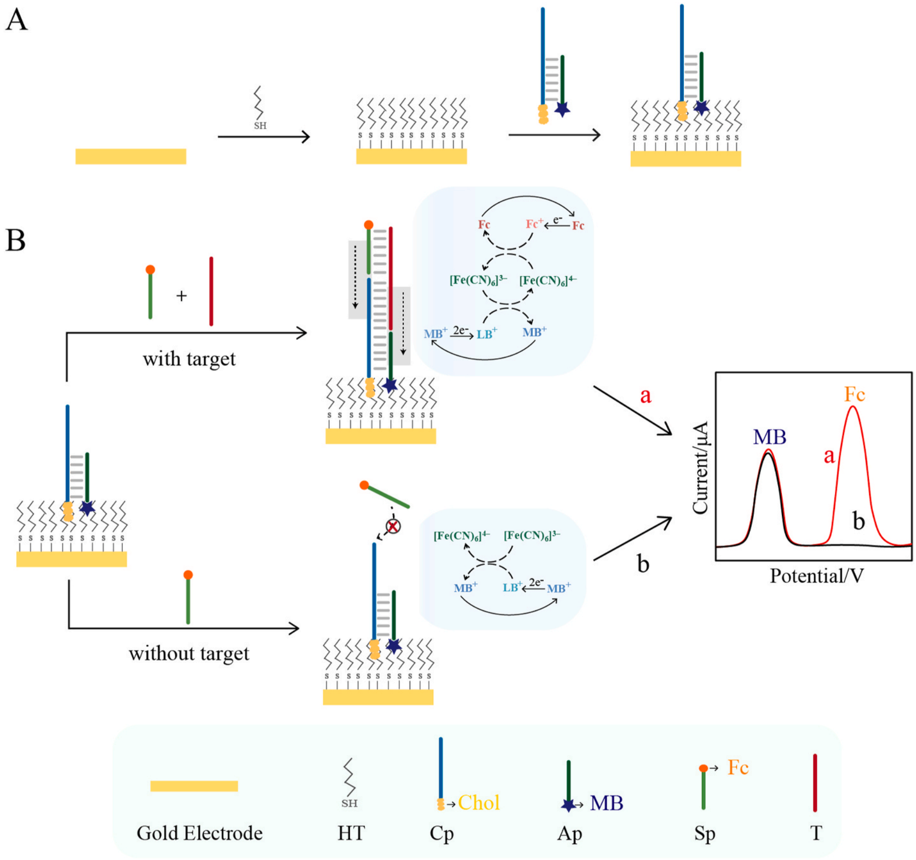

Fig. 5. (A) Schematic of the Cp-Ap-anchored electrode. (B) Schematic of a base-stacking-driven ratiometric electrochemical biosensor using dsDNA-mediated MB-and-Cholesterol co-immobilization for sensitive detection of T.

$[Fe(CN)_6]^{4-}$, which then reduces Fc^+ back to its original state (Fc). This regenerative cycle facilitates the redox of $Fc\text{-}Fc^+$. The regenerated $[Fe(CN)_6]^{3-}$ can re-catalyze the redox of $MB^+\text{-}LB^+$, creating a cascade in the electrocatalytic reaction (Fig. S15C).

Based on the HT SAM, a cascade electrocatalytic reaction of MB and Fc mediated by $[Fe(CN)_6]^{3-}$ can be achieved. In addition to serving as a DNA probe immobilizer, MB can also serve as an internal reference within the assembly electrode, reducing signal drift and improving detection precision. To verify this, we constructed a non-ratiometric model and a ratiometric model (Fig. 4E). We compared the signal drift levels of five repeated experiments for both models. As shown in Fig. 4F, the response in the non-ratiometric E-sensor varied greatly across the five tests, with an average relative standard deviation (RSD) of 9.3%. In contrast, the signal response in the ratiometric E-sensor showed significantly less variation, with an RSD of 3.2%. The ratiometric approach was far more robust, reliable, and reproducible than the previous approach that relied on electrochemical “absolute values”.

3.6. *Construction of the ratiometric E-sensor*

SARS-CoV-2 has caused devastating loss of human lives and disruptions to the global economy (Chakraborty and Maity, 2020; Florindo et al., 2020). The most effective strategy to control the pandemic is suppressing virus spread through early detection of infections. Therefore, developing a convenient, rapid, accurate, and sensitive methods for rapid screening of SARS-CoV-2 is highly desired. To this end, based on the above findings, we developed a base-stacking-driven ratiometric electrochemical biosensor using dsDNA-mediated MB-and-Cholesterol co-immobilization for highly sensitive detection of T (SARS-CoV-2 N gene-related fragments). The working principle is illustrated in Fig. 5. First, the electrode is immobilized with HT by Au-S bonding to form a compact HT SAM. The pre-hybridized Cp-Ap complex (modified with cholesterol and MB, respectively) is then anchored to the HT SAM through the hydrophobic interaction of the terminal cholesterol and MB with HT SAM (Fig. 5A). Sp labeled with Fc is designed to specifically recognize T, based on the principle of complementary base pairing. When T is present, it hybridizes with Sp to form Sp-T with a short overhanging. Driven by base-stacking, Sp-T is rapidly captured by Cp-Ap on the interface to form a stable hybrid complex, which brings the modified Fc on Sp to the electrode interface. Upon applying voltage, a large number of MB and Fc molecules react with solution-borne $[Fe(CN)_6]^{3-}$ to produce significant MB and Fc current signals. On the contrary, when T is absent, Sp cannot be captured by Cp-Ap on the electrode interface, and no Fc signal can be detected (Fig. 5B). Eventually, the current signal ratio of Fc to MB is calculated to achieve sensitive and rapid detection of T.

3.7. *Feasibility characterization of the ratiometric E-sensor*

NUPACK software was used to analyze the rationality of the DNA sequence design for the E-sensor (Zadeh et al., 2011). As shown in Fig. S17, when Cp and Ap were mixed, Cp-Ap double-stranded complex with a short overhanging was formed. The theoretical equilibrium concentration (EC) of Cp-Ap was 1 μM (Fig. S17A), which was consistent with the initial concentration of Cp and Ap, indicating that Cp could hybridize with Ap and the theoretical hybridization efficiency was 100%. When Cp, Ap, Sp and T were mixed, the EC of Cp-Ap-Sp-T complex was 0.99 μM, with a hybridization efficiency of 99%. This demonstrated that when T was present, a double-stranded structure (Cp-Ap-Sp-T) was formed (Fig. S17B). In contrast, when Cp, Ap, and Sp were mixed without T, only Sp and Cp-Ap were formed, and the EC of Cp-Ap and Sp were both 1 μM (Fig. S17C), indicating that Cp-Ap could

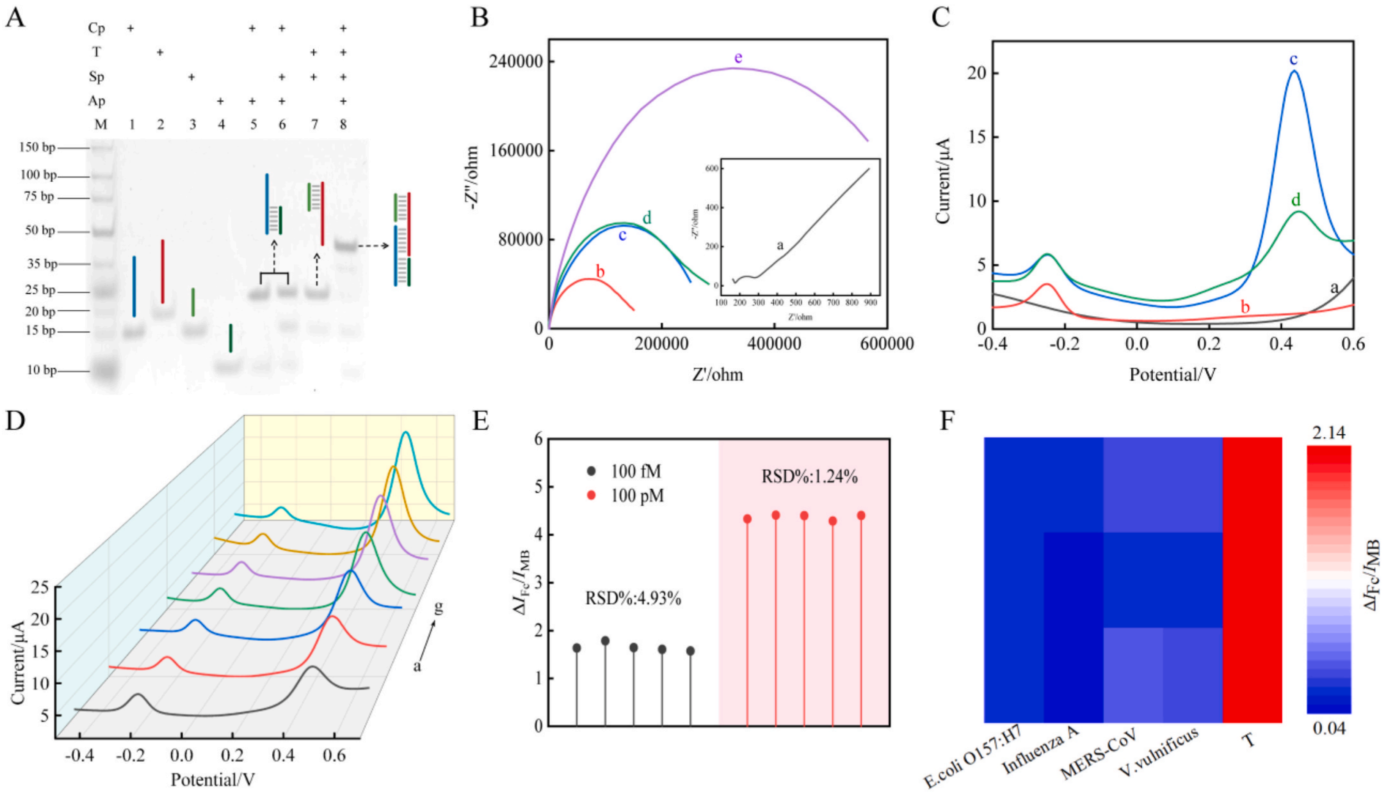

Fig. 6. (A) PAGE characterization of ratiometric E-sensor. Lane M is for the marker; “+” indicates the presence of the strand (Cp, T, Sp, and/or Ap) in the lane. (B) EIS characterization of ratiometric E-sensor (curves a to e are GE, GE/HT, GE/HT/Cp-Ap, GE/HT/Cp-Ap/Sp, GE/HT/Cp-Ap/Sp-T, respectively). (C) SWV characterization of ratiometric E-sensor (curves a to d are GE/HT, GE/HT/Cp-Ap, GE/HT/Cp-Ap/Sp-T, GE/HT/Cp-Ap/Sp, respectively). (D) Signal response of the ratiometric E-sensor under different concentrations of T (The concentrations of T in curves a to g are: 0 fM, 10 fM, 10^2 fM, 10^4 fM, 10^5 fM, 10^6 fM, 10^7 fM). (E) The reproducibility of ratiometric E-sensor. (F) The specificity of ratiometric E-sensor.

not capture Sp in the absence of T. The above results demonstrated the theoretical feasibility of the E-sensor.

Polyacrylamide gel electrophoresis (PAGE) was used to provide experimental evidence for the feasibility of the E-sensor (Fig. 6A). Electrophoretic bands in lanes 1–4 were for Cp, T, Sp, and Ap, respectively. When Cp and Ap were present, a new band higher than Cp and Ap appeared in lane 5, indicating that Cp could hybridize with Ap. When Cp, Ap, and Sp were mixed, two bands for Cp-Ap and Sp were observed in lane 6, indicating that Cp-Ap could not capture Sp in the absence of T. Furthermore, lane 7 showed a band higher than lane 2 and lane 3, indicating the hybridization of Sp with T. However, when Cp, Ap, Sp, and T were mixed, a new band appeared in lane 8, significantly higher than those in lanes 1–5. This observation suggested that in the presence of T, Sp and T could be captured by Cp-Ap to form the Cp-Ap-Sp-T hybrid complex.

The stepwise fabrication of the ratiometric E-sensor was monitored by EIS. As shown in Fig. 6B, the R_{et} of bare electrode was the lowest (curve a). After the assembly of HT (curve b) and Cp-Ap (curve c), the R_{et} gradually increased, indicating that Cp-Ap was successfully immobilized on the HT-assembled electrode. In the absence of T, Sp cannot hybridize with Cp-Ap, so R_{et} values barely changed (curve d). However, when T was present, Sp hybridized with T to form Sp-T, which was captured by Cp-Ap on the electrode interface, resulting in a large attachment of Cp-Ap-Sp-T to the electrode interface, and R_{et} value increased significantly (curve e). The results confirmed that the ratiometric E-sensor was successfully assembled on the electrode interface and the E-sensor was feasible for target detection.

SWV method was used to further verify the feasibility of the E-sensor for target detection. As shown in Fig. 6C, no redox peak of MB and Fc at HT SAM were observed (curve a). However, as Cp-Ap was further assembled at the electrode interface, MB on the Ap reacted with $[Fe(CN)_6]^{3-}$ to produce a significant current signal (curve b). Subsequently, in the presence of T, Sp and T were captured by Cp-Ap at the electrode interface, forming a large number of Cp-Ap-Sp-T complexes, and a large amount of Fc was introduced into the electrode interface. Under voltage, MB and Fc on the Cp-Ap-Sp-T complexes reacted with $[Fe(CN)_6]^{3-}$ in solution to produce a distinct oxidation peak of MB and Fc (curve c). In contrast, in the absence of T, the MB signal (used as a reference) remained almost unchanged, while a lower Fc background current was generated (curve d). The above experimental results confirmed that the sensor can detect target T effectively.

3.8. *Performance assessment*

To optimize the analytical performance, experimental conditions including the concentrations of Sp and Cp-Ap were adjusted for the construction of ratiometric E-sensor (Fig. S18). Under the optimal conditions, the sensitivity of the ratiometric E-sensor was assessed. As shown in Fig. 6D, with the increase of T concentration, the peak current of MB remained nearly constant, while the peak current of Fc increased gradually. The change in the peak current ratio of Fc to MB ($\Delta I_{Fc}/I_{MB}$) and the logarithm of T concentration was well-linear in the concentration range from 10 fM to 10 nM, with the regression equation of $\Delta I_{Fc}/I_{MB} = 0.7634\ (\lg C_T) + 0.1580$ and a correlation coefficient of $r = 0.9998$ (Fig. S19). According to the 3σ rule, the determined limit of detection (LOD) of the E-sensor was 1.32 fM, showing a high sensitivity of the proposed method. The E-sensor outperformed recently reported methods in terms of detection time and sensitivity (Table S2).

The reproducibility of E-sensor was investigated. As shown in Fig. 6E, five parallel detections of T at 100 fM and 100 pM showed RSD of 4.93% and 1.24%, respectively, indicating excellent reproducibility. The selectivity of the sensor was examined, as shown in Fig. 6F, where the detection signal of T was significantly larger than that of other interference sequences, indicating that the E-sensor has great selectivity for the detection of SARS-CoV-2 N gene-related fragments. The hybridization kinetics of the E-sensor were also characterized, and the peak current ratio of the E-sensor increased over time and reached a plateau at about 300-s (Fig. S20).

Finally, to evaluate the performance of the method for detecting biological samples, SARS-CoV-2 N gene-related fragments were dissolved in PBS-diluted saliva samples, quantified using the regression equation, and the measured concentration and recovery were calculated. As shown in Table S3, the recovery rates ranged from 90.00% to 106.00%, with RSDs between 5.27% and 8.27%, suggesting the broad prospect in biological sample application.

4. Conclusion

In the context of the complexity and multifaceted demands of clinical applications, a multi-functional, inclusive and universal platform is particularly important and critical for achieving synergistic integration of functionality and improving the overall quality of E-sensors. In this study, DNA structures work as a “mediator” to bring desired components to the HT SAM “platform”. The inclusivity and versatility of HT SAM allow each component to function optimally and work synergistically, ultimately improving the overall performance of the E-sensor. As a simple model, we developed a base-stacking-driven ratiometric electrochemical biosensor using dsDNA-mediated MB-and-Cholesterol co-immobilization on HT SAM for sensitive detection of SARS-CoV-2. The E-sensor offers several advantages: 1) The synergistic immobilization of cholesterol and MB effectively strengthens the probe’s stability and attachment at the electrode interface. 2) The dsDNA structure can maintain the upright conformation of DNA, enhancing target accessibility and collision probability. Coaxial base-stacking generated by both strands in dsDNA improves the stability of hybrid products, enhancing DNA hybridization efficiency and rate at the interface. 3) Under the mediation of $[Fe(CN)_6]^{3-}$, MB on the interface promotes the electron transfer of Fc, leading to a $[Fe(CN)_6]^{3-}$-mediated cascade electrocatalytic amplification reaction, thereby improving the sensitivity of the E-sensor. 4) The MB on the interface can be used as an internal reference signal, which is equivalent to the internal standard comparison method in chromatographic analysis. It can greatly reduce the background signal drift caused by different electrode interfaces, probe assembly concentrations, and probe degradation and dissociation caused by non-targets, thereby improving the reproducibility of the E-sensor.

The results demonstrated the E-sensor’s good reproducibility, specificity, and high recovery rate in saliva samples. This method offers a simple, cost-effective, precise, rapid, sensitive, and specific detection approach, greatly enhancing the overall performance of the E-sensor. Additionally, this E-sensor is versatile, easily adaptable for detecting other target analytes by simply altering related sequences. It holds promise for point-of-care testing (POCT) in large-scale disease screening.

CRediT authorship contribution statement

Lilan Xu: Writing – original draft, Conceptualization. **Guanyu Chen:** Supervision, Methodology, Data curation. **Jiayan Wu:** Data curation. **Mingzhu Chen:** Validation. **Wenlu Wang:** Data curation. **Zhuhua Chen:** Validation. **Lifang Lin:** Validation. **Weiming Sun:** Methodology, Formal analysis, Data curation. **Xu Yao:** Methodology, Formal analysis, Data curation. **Jianzhong Zhang:** Project administration, Funding acquisition. **Jinghua Chen:** Writing – review & editing, Project administration, Funding acquisition, Formal analysis, Conceptualization. **Xi Zhang:** Writing – review & editing, Project administration, Funding acquisition, Conceptualization.

Declaration of competing interest

The authors declare that they have no known competing financial interests or personal relationships that could have appeared to influence the work reported in this paper.

Acknowledgment

The authors gratefully acknowledge the financial support of the National Natural Science Foundation of China (22207018), Natural Science Foundation of Fujian Province (2020J01999, 2022J01207), Fujian Key Technological Innovation and Industrialization Projects (2024XQ013), Fujian Science and Technology Plan Project (2024Y4004), Fujian Province Joint Funds for the Innovation of Science and Technology (2024Y9104), Talent Introduction Startup Fund of Fujian Medical University (XRCZX2021017), High-level Talent Project of Fujian Medical University (ZLJH2024008). We would like to thank Zhihong Huang and Sishi Chen from the Public Technology Service Center (Fujian Medical University) for technical assistance.

Appendix A. Supplementary data

Supplementary data to this article can be found online at https://doi.org/10.1016/j.bios.2025.117540.

Data availability

Data will be made available on request.

References

Brahman, P.K., Dar, R.A., Pitre, K.S., 2013. DNA-Functionalized electrochemical biosensor for detection of vitamin B1 using electrochemically treated multiwalled carbon nanotube paste electrode by voltammetric methods. Sensors and Actuators B: Chemical 177, 807–812.

Brahman, P.K., Dar, R.A., Pitre, K.S., 2016a. Voltammetric interaction of vitamin B 1 with DNA at multiwalled carbon nanotube paste electrode. J. Saudi Chem. Soc. 20, S236–S240.

Brahman, P.K., Dar, R.A., Pitre, K.S., 2016b. Voltammetric study of ds-DNA–flutamide interaction at carbon paste electrode. Arab. J. Chem. 9, S1884–S1888.

Brahman, P.K., Dar, R.A., Tiwari, S., Pitre, K.S., 2012. Electrochemical behavior of gatifloxacin at multi-walled carbon nanotube paste electrode and its interaction with DNA. Rev. Anal. Chem. 31 (2).

Cai, S., Lau, C., Lu, J., 2011. Turn-On aptameric system for simple and selective detection of protein via base stacking-dependent DNA hybridization event. Anal. Chem. 83 (15), 5844–5850.

Chakraborty, I., Maity, P., 2020. COVID-19 outbreak: migration, effects on society, global environment and prevention. Sci. Total Environ. 728, 138882.

Chang, K., Fang, Y., He, P., Zhu, C., Liu, X., Zheng, D., Chen, D., Liu, C., 2023. Employing the anchor DSPE-PEG as a redox probe for ratiometric electrochemical detection of surface proteins on extracellular vesicles with aptamers. Anal. Chem. 95 (44), 16194–16200.

Chen, G., Chen, W., Xu, L., Jin, H., Sun, W., Lan, J., Wu, F., Zhang, X., Zhang, J., Chen, J., 2022. Sensitive, highly stable, and anti-fouling electrode with hexanethiol and Poly-A modification for exosomal microRNA detection. Anal. Chem. 94 (13), 5382–5391.

Chen, G., Yang, N., Xu, L., Lu, S., Chen, Z., Wu, F., Chen, J., Zhang, X., 2023. Base-stacking-driven catalytic hairpin assembly: a nucleic acid amplification reaction using electrode interface as a "Booster" for SARS-CoV-2 Point-of-Care testing. Anal. Chem. 95 (42), 15595–15605.

Chen, Y., Song, Y., Wang, X., Tang, H., Li, C., 2024. Genetically engineered virus-like particle-armoured and multibranched DNA scaffold-corbelled ultra-sensitive hierarchical hybridization chain reaction for targeting-enhanced imaging in living biosystems under spatiotemporal light powering. Biosens. Bioelectron. 247.

Cheng, L., He, Y., Yang, Y., Su, C., He, H., You, M., Chen, J., Lin, Z., Hong, G., 2023. Highly specific and sensitive sandwich-type electrochemiluminescence biosensor for HPV16 DNA detection based on the base-stacking effect and bovine serum albumin carrier platform. Biosens. Bioelectron. 241.

Deng, C., Pi, X., Qian, P., Chen, X., Wu, W., Xiang, J., 2017. High-performance ratiometric electrochemical method based on the combination of signal probe and inner reference probe in one hairpin-structured DNA. Anal. Chem. 89 (1), 966–973.

Florindo, H.F., Kleiner, R., Vaskovich-Koubi, D., Acúrcio, R.C., Carreira, B., Yeini, E., Tiram, G., Liubomirski, Y., Satchi-Fainaro, R., 2020. Immune-mediated approaches against COVID-19. Nat. Nanotechnol. 15 (8), 630–645.

Hu, P., Li, M., Wei, X., Yang, B., Li, Y., Li, C.-Y., Du, J., 2018. Cooperative toehold: a mechanism to activate DNA strand displacement and construct biosensors. Anal. Chem. 90 (16), 9751–9760.

Huang, W., Wu, X., Fu, J., Ye, J., Gao, J., Yuan, R., Xu, W., 2024a. Sensitive electrochemical biosensor for Ustilaginoidea virens short-stranded DNA segment via higher-ordered G-quadruplex multimerization induced by LAMP/H+-responsive i-motif folding. Sensors and Actuators B: Chemical 411.

Huang, Z., Zhang, L., Dou, Y., Liu, X., Song, S., Jiang, H., Fan, C., 2024b. Electrochemical biosensor for point-of-care testing of low-abundance biomarkers of neurological diseases. Anal. Chem. 96 (25), 10332–10340.

Kuralay, F., Campuzano, S., Wang, J., 2012. Greatly extended storage stability of electrochemical DNA biosensors using ternary thiolated self-assembled monolayers. Talanta 99, 155–160.

Lao, R., Song, S., Wu, H., Wang, L., Zhang, Z., He, L., Fan, C., 2005. Electrochemical interrogation of DNA monolayers on gold surfaces. Anal. Chem. 77 (19), 6475–6480.

Li, H., Arroyo-Currás, N., Kang, D., Ricci, F., Plaxco, K.W., 2016. Dual-reporter drift correction to enhance the performance of electrochemical aptamer-based sensors in whole blood. J. Am. Chem. Soc. 138 (49), 15809–15812.

Li, Q., Liu, L., Mao, D., Yu, Y., Li, W., Zhao, X., Mao, C., 2020. ATP-Triggered, allosteric self-assembly of DNA nanostructures. J. Am. Chem. Soc. 142 (2), 665–668.

Li, S., Wang, Y., Zhang, Z., Wang, Y., Li, H., Xia, F., 2021. Exploring end-group effect of alkanethiol self-assembled monolayers on electrochemical aptamer-based sensors in biological fluids. Anal. Chem. 93 (14), 5849–5855.

Li, Z., Jin, R., Mirkin, C.A., Letsinger, R.L., 2002. Multiple thiol-anchor capped DNA-gold nanoparticle conjugates. Nucleic Acids Res. 30 (7), 1558–1562.

Lu, B., Ohayon, Y.P., Woloszyn, K., Yang, C.-f., Yoder, J.B., Rothschild, L.J., Wind, S.J., Hendrickson, W.A., Mao, C., Seeman, N.C., Canary, J.W., Sha, R., Vecchioni, S., 2023. Heterobimetallic base pair programming in designer 3D DNA crystals. J. Am. Chem. Soc. 145 (32), 17945–17953.

Mohammadniaei, M., Zhang, M., Ashley, J., Christensen, U.B., Friis-Hansen, L.J., Gregersen, R., Lisby, J.G., Benfield, T.L., Nielsen, F.E., Henning Rasmussen, J., Pedersen, E.B., Olinger, A.C.R., Kolding, L.T., Naseri, M., Zheng, T., Wang, W., Gorodkin, J., Sun, Y., 2021. A non-enzymatic, isothermal strand displacement and amplification assay for rapid detection of SARS-CoV-2 RNA. Nat. Commun. 12 (1), 5089.

Myres, G.J., Harris, J.M., 2023. Stable immobilization of DNA to silica surfaces by sequential michael addition reactions developed with insights from confocal raman microscopy. Anal. Chem. 95 (6), 3499–3506.

Nazir, F., Tabish, T.A., Tariq, F., Iftikhar, S., Wasim, R., Shahnaz, G., 2022. Stimuli-sensitive drug delivery systems for site-specific antibiotic release. Drug Discov. Today 27 (6), 1698–1705.

Romanò, S., Angelillo, A., Cimmino, W., Iaccarino, N., Nele, V., Campani, V., De Rosa, G., Cinti, S., 2024. An electrochemical strip to evaluate and to discriminate drug encapsulation in lipid nanovectors. Anal. Chem. 96 (29), 11651–11656.

Shaver, A., Arroyo-Currás, N., 2022. The challenge of long-term stability for nucleic acid-based electrochemical sensors. Curr. Opin. Electrochem. 32.

Shaver, A., Curtis, S.D., Arroyo-Currás, N., 2020. Alkanethiol monolayer end groups affect the long-term operational stability and signaling of electrochemical, aptamer-based sensors in biological fluids. ACS Appl. Mater. Interfaces 12 (9), 11214–11223.

Singhana, B., Jamison, A.C., Hoang, J., Lee, T.R., 2013. Self-assembled monolayer films derived from tridentate cyclohexyl adsorbates with alkyl tailgroups of increasing chain length. Langmuir 29 (46), 14108–14116.

Tu, J., Min, J., Song, Y., Xu, C., Li, J., Moore, J., Hanson, J., Hu, E., Parimon, T., Wang, T.-Y., Davoodi, E., Chou, T.-F., Chen, P., Hsu, J.J., Rossiter, H.B., Gao, W., 2023. A wireless patch for the monitoring of C-reactive protein in sweat. Nat. Biomed. Eng. 7 (10), 1293–1306.

Wan, J., Liang, Y., Hu, Q., Liang, Z., Feng, W., Tian, Y., Li, S., Ye, Z., Hong, M., Han, D., Niu, L., 2023. Amplification-free ratiometric electrochemical aptasensor for point-of-care detection of therapeutic monoclonal antibodies. Anal. Chem. 95 (37), 14094–14100.

Wang, L., Wang, X., Chen, X., Liu, J., Liu, S., Zhao, C., 2012. Development of an electrochemical DNA biosensor with the DNA immobilization based on in situ generation of dithiocarbamate ligands. Bioelectrochemistry 88, 30–35.

Wang, M., Yang, Y., Min, J., Song, Y., Tu, J., Mukasa, D., Ye, C., Xu, C., Heflin, N., McCune, J.S., Hsiai, T.K., Li, Z., Gao, W., 2022a. A wearable electrochemical biosensor for the monitoring of metabolites and nutrients. Nat. Biomed. Eng. 6 (11), 1225–1235.

Wang, X., Shan, M., Zhang, S., Chen, X., Liu, W., Chen, J., Liu, X., 2022b. Stimuli-responsive antibacterial materials: molecular structures, design principles, and biomedical applications. Adv Sci (Weinh) 9 (13), e2104843.

Wu, P., Fang, N., Tao, Y., Wang, Y., Jia, W., Zhang, H., Cai, C., Zhu, J.-J., 2023. Enhancing the reliability of SERS detection in ampicillin using oriented tetrahedral framework nucleic acid probes and a long-range SERS substrate. Anal. Chem. 95 (38), 14271–14278.

Xia, Y., Chen, T., Zhang, L., Zhang, X., Shi, W., Chen, G., Chen, W., Lan, J., Li, C., Sun, W., Chen, J., 2021. Colorimetric detection of exosomal microRNA through switching the visible-light-induced oxidase mimic activity of acridone derivate. Biosens. Bioelectron. 173.

Xia, Y., He, W., Li, J., Zeng, L., Chen, T., Liao, Y., Sun, W., Lan, J., Zhuo, S., Zhang, J., Yang, H., Chen, J., 2019. Acridone derivate simultaneously featuring multiple functions and its applications. Anal. Chem. 91 (13), 8406–8414.

Zadeh, J.N., Steenberg, C.D., Bois, J.S., Wolfe, B.R., Pierce, M.B., Khan, A.R., Dirks, R.M., Pierce, N.A., 2011. NUPACK: analysis and design of nucleic acid systems. J. Comput. Chem. 32 (1), 170–173.

Zeng, X., Wu, C., Xiong, Y., Zhan, Z., Shen, C., Lin, F., Zhang, J., Chen, P., 2024. Target proteins-regulated DNA nanomachine-electroactive substance complexes enable separation-free electrochemical detection of clinical exosome. Biosens. Bioelectron. 256, 116273.

Zhang, P., Jiang, J., Yuan, R., Zhuo, Y., Chai, Y., 2018. Highly ordered and field-free 3D DNA nanostructure: the next generation of DNA nanomachine for rapid single-step sensing. J. Am. Chem. Soc. 140 (30), 9361–9364.

Zhang, R., Liu, J., Li, Y., 2019. MXene with great adsorption ability toward organic dye: an excellent material for constructing a ratiometric electrochemical sensing platform. ACS Sens. 4 (8), 2058–2064.

Zhang, S., Li, W., Luan, J., Srivastava, A., Carnevale, V., Klein, M.L., Sun, J., Wang, D., Teora, S.P., Rijpkema, S.J., Meeldijk, J.D., Wilson, D.A., 2023. Adaptive insertion of a hydrophobic anchor into a poly(ethylene glycol) host for programmable surface functionalization. Nat. Chem. 15 (2), 240–247.

Zhao, X., Yao, Q., Long, S., Chi, W., Yang, Y., Tan, D., Liu, X., Huang, H., Sun, W., Du, J., Fan, J., Peng, X., 2021. An approach to developing cyanines with simultaneous intersystem crossing enhancement and excited-state lifetime elongation for photodynamic antitumor metastasis. J. Am. Chem. Soc. 143 (31), 12345–12354.